

Overcoming the limitations of patch-based learning to detect cancer in whole slide images

Ozan Ciga^{a,*}, Tony Xu^{e,1}, Sharon Nofech-Mozes^{c,d}, Shawna Noy^b, Fang-I Lu^{c,d}, Anne L. Martel^{a,b}

^a*Department of Medical Biophysics, University of Toronto, Canada*

^b*Sunnybrook Research Institute, Toronto, Canada*

^c*Department of Laboratory Medicine and Molecular Diagnostics, University of Toronto, Canada*

^d*Division of Anatomic Pathology, Sunnybrook Health Science Center, Toronto, Ontario, Canada*

^e*Department of Electrical and Computer Engineering, University of British Columbia, Canada*

Abstract

Whole slide images (WSIs) pose unique challenges when training deep learning models. They are very large which makes it necessary to break each image down into smaller patches for analysis, image features have to be extracted at multiple scales in order to capture both detail and context, and extreme class imbalances may exist. Significant progress has been made in the analysis of these images, thanks largely due to the availability of public annotated datasets. We postulate, however, that even if a method scores well on a challenge task, this success may not translate to good performance in a more clinically relevant workflow. Many datasets consist of image patches which may suffer from data curation bias; other datasets are only labelled at the whole slide level and the lack of annotations across an image may mask erroneous local predictions so long as the final decision is correct. In this paper, we outline the differences between patch or slide-level classification versus methods that need to localize or segment cancer accurately across the whole slide, and we experimentally verify that best practices differ in both cases. We apply a binary cancer detection network on post neoadjuvant therapy breast cancer WSIs to find the tumor bed outlining the extent of cancer, a task which requires sensitivity and precision across the whole slide. We extensively study multiple design choices and their effects on the outcome, including

*Corresponding author: e-mail: ozan.ciga@mail.utoronto.ca

¹This work was conducted while the author was doing internship at Sunnybrook Research Institute.

architectures and augmentations. Furthermore, we propose a negative data sampling strategy, which drastically reduces the false positive rate (7% on slide level) and improves each metric pertinent to our problem, with a 15% reduction in the error of tumor extent.

Keywords: clustering, residual cancer burden, tumor bed estimation, representation learning

1. Introduction

Convolutional neural networks (CNNs) are able to extract features from raw images, which has made them attractive in many visual tasks, including medical image analysis. In computational pathology, current approaches mostly focus on isolated patches extracted from WSIs, or tasks that are tailored around a slide or patient-level predictions, as opposed to requiring consistently high precision and sensitivity across a WSI (Srinidhi et al., 2019). We argue that applying CNNs on WSIs might not achieve similar performances due to several biases outlined below, in addition to the different characteristics of WSIs and patches extracted from WSIs.

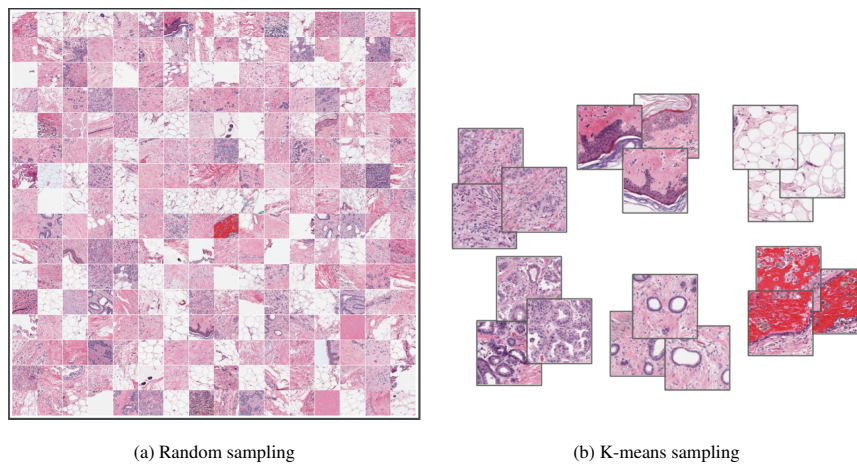


Figure 1: Negative mining with random sampling versus feature based K-means clustering from whole-slide images. Both figures are extracted from actual experiments. In Fig. 1b, we show the three samples closest to the centres of six randomly selected clusters for illustration.

Much of the early work in digital pathology involved the extraction of a small fraction of patches from each WSI, which were then annotated or labelled by pathologists. This approach is vulnerable to a data curation bias which refers to the implicit assumptions made by curators that may affect the task outcome. In patch-level problems, training and validation datasets are generally collected by the same experts or with the same instructions. For example, both training and validation sets contain the same number of unique classes with similar ratios. Data curation is also generally biased towards the positive class since these images are usually collected from patients undergoing treatment. Curation bias is exploited for tuning the network hyperparameters (e.g., the confidence threshold) on validation sets to maximize performance on the held-out test set. While these are appropriate in the context of a challenge, they do not necessarily hold for tasks with WSIs, where it is not possible to determine a universally best threshold or to comprehensively annotate data (e.g., representing all negatives in cancer detection, such as ink, creases, out-of-focus regions or non-cancerous tissue).

Although CNNs can only be applied to individual patches within a WSI, slide level tasks can be performed by aggregating the individual patch level results. It is, however, important to take into account how this aggregation is carried out when evaluating and comparing algorithms. Many tasks that involve WSIs are binary decision problems or allow a number of errors without negatively impacting the measured metric. For instance, Bandi et al. (2018) aim to determine the severity of breast cancer by measuring the extent of metastasis via a five-class problem. However, if a single macro-metastasis is identified, the exact number of metastases become irrelevant for certain classes by definition. Similarly, Campanella et al. (2019) aim to determine whether cancer is present or not present in a WSI. On slides labelled as containing cancer, false positive are not penalized because the location of the detected cancer is not important; conversely, in slides labelled as negative, there is no differentiation between one or many false positive detections. In contrast, the number of errors at the patch level will be related directly to task performance in slide level tasks that involve quantification or segmentation.

CNNs usually work best with small images such as 224×224 pixels, whereas a WSI can be $100,000 \times 100,000$ pixels. Even a drastic down-sampling (e.g., $16 \times$) will neces-

sitate tiling and working on a portion of the WSI. Modifying the architecture, or simply feeding a larger image to overcome this issue is not always possible due to optimization challenges and graphical memory constraints. While the latter is less prohibitive and may be mitigated by technological advancements, training models with more parameters to accommodate WSIs with larger convolutional kernels are infeasible due to $O((\text{kernel side length})^2)$ scaling. This upper bounds the performance on WSIs since CNNs heavily rely on context and edges, which may not always be present, especially when the WSI is viewed under high resolution (e.g., the outline of a gland or duct may only be partially available if the images are sampled at high resolution over a limited field of view).

In this paper, we extensively study the differences between WSI analysis and patch level analysis. We use WSIs of breast tissue which has been surgically resected following neoadjuvant therapy (NAT) to explore the differences between the following three tasks:

1. Patch-level classification: determine whether cancer cells are present or not in a curated set of patches from WSIs (Martel et al., 2019).
2. Slide-level classification: determine whether a WSI contains cancer cells or not without localizing the cancer within the WSI.
3. Slide-level segmentation: Find the convex hull that contains all cancer cells in a WSI (i.e., the tumor bed estimation).

Importantly, a binary classification network is used in each task. For the segmentation task, the WSI is tiled into patches, and each patch is classified as cancer or no cancer prior to computing the convex hull. We observe that the best practices, including the most suitable augmentations and the appropriate network complexity, are different for each task. We find a network achieving $> 99\%$ F1 score on patch-level classification fails to identify the tumor bed accurately, with a Dice score of $\sim 50\%$. We then study failure points of the patch-level classifier and propose a novel negative sampling method that improves the task performance beyond random or no sampling. We also observe a large gap between slide-level classification and segmentation. For the former, we achieve 94% accuracy, whereas for the latter, we obtain a Dice score of 75% .

2. Problem definition

To exemplify the differences between patches and WSIs, we tackle the automatic detection of breast cancer. Breast cancer is the second most common invasive cancer in women, where around 12% of women having a lifetime risk of getting breast cancer (DeSantis et al., 2014). New therapies have improved outcomes and it is increasingly important to assess the stage and subtype of cancer more precisely in order to select the most appropriate treatment. While tools that can identify and characterize cancer in a specific region of the tissue specimen selected by a pathologist have value, there is a need for automated tools capable of processing WSIs since cancer may be anywhere within a slide, or even spread across multiple slides.

An evaluation of the residual tumour in surgically resected breast tissue after neoadjuvant therapy for breast cancer is clinically relevant in determining treatment response and estimating prognosis. It has been shown that the extent of the residual tumor bed, the cellularity within the tumor bed, and the presence or absence of lymph node metastases can be used to estimate the five-year recurrence risk (Symmans et al., 2007, 2017). While automated analysis of WSIs for breast cancer tasks is common (Ehteshami Bejnordi et al., 2017; Bandi et al., 2018; Aresta et al., 2019), there have been few studies that focus on post-NAT images or slide-wide analysis (Akbar et al., 2019). Recently, (Campanella et al., 2019) conducted a large scale study with 9894 slides from axillary lymph nodes for breast cancer metastasis detection, and achieved 0.989 area under the curve (AUC). 52% of the false negatives were from slides that showed signs of neoadjuvant chemotherapy, indicating the challenges associated with identifying cancer in post neoadjuvant therapy images, even when the dataset size is large. In addition, 8.6% of false negatives were due to isolated single tumor cells, which play an important role in determining the tumor bed outline as they may change the extent significantly.

Due to its non-trivial nature, clinical relevance and sensitivity towards both false positives and negatives, we conduct experiments for the tumor bed estimation task on WSIs of resected breast tissue. The tumor bed is defined as the convex hull that contains all residual cancer cells and the task requires that all residual cancer cells are detected; after therapy this is more difficult as isolated cancer cells may be surrounded by stromal

tissue. The task also requires a very low false positive detection rate as the erroneous detection of cancer cells can lead to large errors in the boundaries of the tumor bed.

3. Methods

3.1. Data

The BreastPathQ training dataset (Akbar et al., 2019) consists of 2394 patches (of size 512×512) extracted from 69 WSIs of Post-NAT-BRCA specimens (Peikari et al., 2017). BreastPathQ images are given labels according to the percentage of cellularity in each patch. The training set is imbalanced, where 71% of the images are tumor-positive. The corresponding WSIs (Martel et al., 2019) also include tumor bed outlines for each slide which we use for sampling additional negative patches from tumor-free regions of the WSIs.

We use the testing images from the BreastPathQ challenge for the patch-level classification task. This set includes 1106 images, and is annotated by two independent pathologists. The test set for the slide-level classification and segmentation tasks is composed of a private set of 50 WSIs, evenly and randomly sampled from 10 independent cancer patients in different treatment stages. Three pathologists have independently annotated tumor bed outlines in each WSI and later reviewed each WSI together to create a consensus ground truth; this allows us to assess the inter-expert disagreement rate. In our experiments, we use the consensus ground truth unless otherwise stated. According to the consensus dataset, 30% of the WSIs are tumor-free.

3.2. Preprocessing

Regions without nuclei are not relevant in identifying tumors. Therefore, we threshold each WSI in HSV color space to remove such regions, with $0.65 > hue > 0.5$, $saturation > 0.1$, and $0.9 > value > 0.5$. These bounds are experimentally determined using a separate public dataset for breast cancer segmentation (Aresta et al., 2019). We tile the WSI and pass patches with foreground ratios $\geq 25\%$ through the model during the evaluation stage.

3.3. Patch-level classification task

We use the BreastPathQ dataset for patch-level classification. The continuous cellularity percentage values per patch are mapped to two classes, with cellularity percentages above zero labelled as cancer.

3.4. Slide-level tasks

In addition to the same dataset used for patch-level classification, we incorporate additional negative (no cancer) samples for the slide level tasks (see Section 3.5 for details).

Our method achieves slide-level segmentation (tumor bed estimation) by tiling the WSI into distinct patches and generating a probability value (of being tumor-positive) per patch. One may slide a window in strides smaller than the patch length to improve the classification of each pixel through a voting scheme. For example, given a patch size of 512, a stride of 256 will generate four separate probability values per pixel, representing if the patch contains any tumor. Then, these values may be averaged to obtain more accurate probability values per pixel. Since each value is obtained using a different patch, striding helps to incorporate context better.

The predicted label for the slide-level classification can be obtained from the segmentation output. Specifically, if the tumor bed exists, or there is one or more positive patch on the WSI, the WSI is labeled as tumor-positive.

3.5. Negative sampling

A single WSI may contain artifacts (e.g., creases, random blurring of regions, ink or staining residues), as well as structures that are considered as background (e.g., histocytes, adenosis, or red blood cells in tumor bed estimation) which may not have been filtered out in the preprocessing step. While all datasets provide negative samples, it is not feasible to label all forms of negatives. Therefore in digital histopathology, it is common for the negative (e.g., healthy or benign tissue in breast cancer detection) class to be underrepresented.

BreastPathQ dataset consists of 69 WSIs, where each WSI is annotated for the tumor bed outline. By definition, patches extracted from outside of the tumor bed

region are considered as completely cancer-free. We sample patches from outer extents of each WSI and collect a total of 1.4 million images. Then, we sample 21 thousand images randomly or by clustering. For clustering, we use features ($\in \mathbb{R}^{1280}$) generated by EfficientNet-B0 model trained on ImageNet (Tan and Le, 2019). Specifically, we use features corresponding to each image obtained by 2d-average pooling of the final layer of the network prior to the fully-connected classification layer (also called as the pre-activation). We then cluster 1.4 million feature vectors into three thousand clusters using the mini-batch K-means algorithm and select seven instances from each cluster. Examples of sampled images from both random and K-means sampling strategies can be viewed in Fig. 1.

4. Experiments

4.1. Experimental setup

For all experiments, we use the EfficientNet framework (Tan and Le, 2019), and train the network for predicting if a patch of size 224×224 (training patches are of size 512×512 , which are randomly cropped to 448×448 before resizing each dimension in half) contains cancer cells. EfficientNet is based on AutoML framework and compound scaling, and achieves better performance than standard architectures such as residual networks with a fewer number of trainable parameters. We use Adam optimizer with $\beta_1 = 0.9$, $\beta_2 = 0.999$, learning rate of 0.0001, batch size of 20, and weighted cross-entropy loss function, and train for 250 epochs for each experiment. We split 15% of the training data for validation, and select the model with minimum validation loss in testing. Unless otherwise stated, we use the EfficientNet-B0 model.

4.2. Metrics

In binary decision problems, such as determining *any* presence of tumor in WSIs, finding a single positive region suffices for identifying the positive WSIs, and any additional false positives or false negatives for the same WSI do not incur any penalty. In contrast, our task requires us to be consistently precise throughout the WSI in order to estimate the tumor bed accurately. Therefore, we report both the confusion matrix

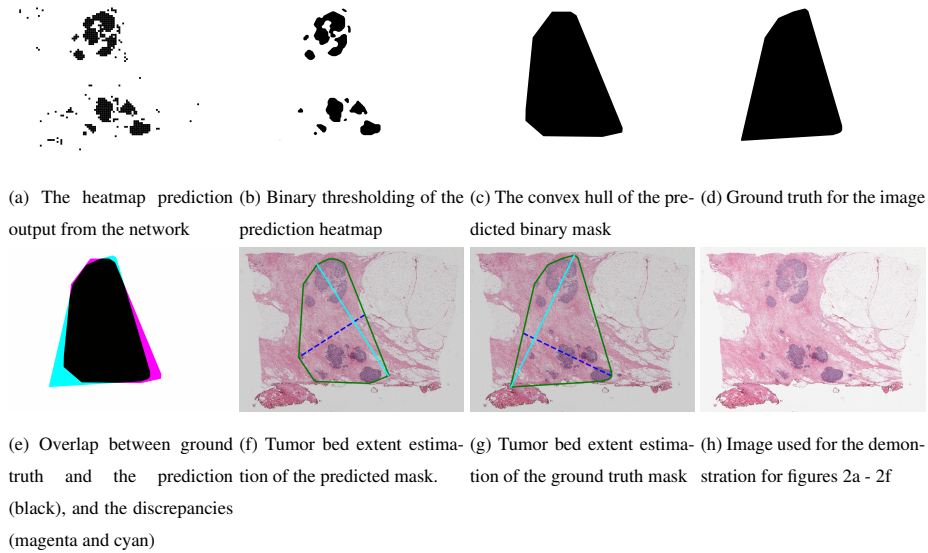


Figure 2: Comparing overlap (Dice coefficient) and difference between ground truth and the prediction in $d_{prim} = \sqrt{d_1 d_2}$, where d_1 is the primary or the longest (turquoise), and d_2 is the secondary (blue) diagonal. The process is visualized from left to right, then top to bottom (row major order).

to quantify if our system is able to detect tumor accurately or discard slides without tumor, as well as the error in d_{prim} (see Fig. 2 for visualization and Appendix A for details), defined as the absolute difference between the prediction and ground truth averaged over the test set, and the overlap (measured by the Dice coefficient) between the ground truth and the prediction. Note that d_{prim} is especially important in assessing the quality of predictions since, unlike the Dice coefficient, this metric is very sensitive to distant false positives and false negatives towards the WSI’s outer edges.

For our purposes, the confusion matrix is related to the slide-level classification task, whereas the Dice coefficient and d_{prim} are related to the slide-level segmentation task. Importantly, segmentation-related metrics are not calculated for WSIs where no tumour is detected. This means that a lower error in d_{prim} may be due to the exclusion of WSIs that are falsely classified as negative for residual tumour when calculating the average value.

Table 1: Binary (tumor vs. no tumor) classification accuracies on BreastPathQ test set with different negative sampling schemes using minority oversampling.

Negative sam- pling	Acc.	Cfs. mtx.
K-means	92.6%	$\begin{pmatrix} 173 & 58 \\ 23 & 852 \end{pmatrix}$
Random	96.3%	$\begin{pmatrix} 200 & 31 \\ 9 & 866 \end{pmatrix}$
None	98.7%	$\begin{pmatrix} 224 & 7 \\ 7 & 868 \end{pmatrix}$

4.3. Tasks

4.3.1. Patch-level cancer detection

We use models trained with minority oversampling weighing (see Table 3), and assess their performance on patch-level BreastPathQ challenge test set with 1106 samples. We also conduct experiments to assess the effects of augmentation, size of the architecture and number of test time augmentations.

4.3.2. Whole-slide image cancer detection

After separately annotating the test set, pathologists reviewed the dataset together and discarded four slides due to high disagreement rates. In these slides, pathologists disagreed as to the presence of tumor, annotated non-overlapping regions as the tumor bed, or disagreed on highly contentious regions where the presence of tumor could not be determined by only using H&E stained slides. For the remaining slides, a consensus tumor bed was selected using a combination of expert annotations. Any additional regions were not examined during this step.

4.4. Results

4.4.1. Patch image analysis

We compare three different negative sampling methods in Table 1. The negative instances are sampled from the WSIs as described in Section 3.5. Minority oversampling performed the best for all sampling strategies. We compare multiple augmentation strategies, number of test time augmentations (TTA), and the effect of model complexity on the classification performance in Table 2.

4.4.2. Whole slide image analysis

The results of our experiments are presented in tables 3, 4, 5 and 6. Note that the average ground truth d_{prim} is 14.5 millimeters, with a standard deviation of 6.1. We compare the discrepancy between references (i.e., the pathologists) to each other, as well as to the network in Table 7 after the consensus set (with 46 slides) has been established. We also make the same comparison prior to consensus, accounting for all 50 slides in Table 8.

We first determine the best negative sampling method, along with options for weighing different samples depending on their class (Table 3). We compare three different sampling strategies, including the clustering approach defined in Section 3.5, randomly selecting negative instances as well as no additional negative sampling beyond what the training data already has. Negative mining creates an imbalance in favor of the negatives (85% of the training data). Therefore, we use multiple balancing strategies, including multiplying the incurred loss with a coefficient that is directly (\propto) or inversely ($\frac{1}{\propto}$) proportional to its corresponding class. We also conduct experiments using no balancing (=) and balancing by oversampling. For our training data, each negative sample is passed through the network two times, whereas each positive sample is passed 11 times per epoch during the training.

We also compare the effect of different types of image augmentation on slide-level classification and segmentation tasks (Table 4). We compare randomly cropping 448×448 rectangular boxes from the training instances versus no cropping both during training and evaluation. We modify the color properties of each instance by applying color jittering, which amounts to randomly changing brightness, contrast, saturation

and hue values by 5% from their original values, as well as by stain normalization using a reference staining matrix (Macenko et al., 2009). We experiment applying affine image transformations by scaling the cropped patch down or up by 10%, and shearing by 60° in both x and y axes.

We compare four different models with varying widths and depths to understand the effect of model complexity on slide-level task outcomes (Table 5). We also compare multiple sliding window approaches for finding the most suitable tile stride (Table 6). Finally, we compare our method to each of the three pathologists, along with comparing pathologists to each other in tables 7 and 8.

5. Discussion and conclusion

8% of the test set had to be discarded as the three pathologists were unable to reach consensus; this demonstrates the challenge associated with estimating the tumor bed, even for experts. In clinical practice, such challenging cases can be resolved by using an additional stain (e.g., immunostaining). Interestingly, two false positives and two false negative WSIs that our system initially detected were discarded in the consensus set, indicating errors made by the network are not random, and the failure points can be attributed to the uncertainty in the slide.

We find using randomly sampled negative instances to be particularly ineffective in identifying tumor-free slides. In effect, randomly sampling negative regions undersamples rare regions that exist in WSIs. In contrast, clustering negative samples based on a salient feature representation allows us to group visually similar instances. Therefore, clustering lets us sample the negative space more evenly, which improves precision. Furthermore, relying only on annotator labeled negative data (*None* setting) is incapable of identifying true negatives and has a much lower performance compared to either K-means or random sampling. Upon examination of the predictions, we find that the network is incapable of identifying structures such as red blood cells or scanner imperfections (e.g., shadow effects), which are not present in the original BreastPathQ dataset, however negative sampling from Post-NAT BRCA WSIs provide us with this information. While it might not always be possible to obtain a boundary beyond which

there is no cancer present, many datasets contain negative WSIs that can be sampled in a similar fashion.

After incorporating the negative samples, our dataset is highly imbalanced in favor of negative samples (85%). A common strategy in handling class imbalance is to increase the cost of mislabeling the minority class by using weighted cross-entropy, where the weights per class are inversely proportional to the number of training samples with that label. We found that this strategy artificially skews the network to predict more samples from the minority class, which increases the number of false negatives. A counter-intuitive approach, where we use directly proportional weights, performs better, and not accounting for the imbalance (equal weights) gives the best performance out of these three approaches. Finally, we observe that oversampling the minority class to rebalance class distributions gives the best overall performance. Therefore, we use K-means negative samples with minority oversampling in slide-level experiments presented from Table 5 onward. In contrast, the results for the patch-level classification task shown in Table 1 suggest that any form of negative sampling adversely impacts prediction accuracy. Injecting information that is not present in the test set has a negative effect since the network has learned a more complex decision boundary that is not utilized for testing. Interestingly, random sampling is not as detrimental, possibly because most of the negative training instances look significantly different from positives.

We find that randomly cropping the instances improve results in both slide-level segmentation and classification tasks. We find that light color jittering performs better than stain normalization. Affine transformations do not improve results for the WSI task. In patch level analysis, we observe that augmentations are less significant, and that more than two test time augmentations (including random cropping by 448×448 , flips and rotations) negatively impact the prediction accuracy. This is in contrast to WSI level predictions, where a smaller tile stride (corresponding to test-time augmentations in patches) is usually correlated with better performance.

We find that EfficientNet-B3, which is comparable to ResNet34 and ResNet50 in terms of model complexity, provides the best bias and variance trade-off for our data and slide-level tasks. For the patch-level task, we find larger architectures to be more

suitable, where the best performing network (B5) is $2.5\times$ the size of best performing model (B3) for tumor bed estimation.

We find that stride lengths smaller than the patch length primarily help identify negative regions, and marginally improve the tumor bed outlines. We also find that stride lengths drastically smaller than the patch length do not lead to significantly benefit results, and are computationally prohibitive (e.g., a stride length of 16 processes each pixel 1024 times, and each WSI in this setting can have more than a million patches to be evaluated).

In conclusion, we find that best practices in patches versus WSI analysis vary significantly, despite employing the same networks with the same training data. This discrepancy also highlights that the advancements in either setting cannot be directly applied to the other, and independent research is required to further both fields.

Conflict of interest

ALM is co-founder and CSO of Pathcore. Other authors have no conflict to declare.

Acknowledgments

This research was enabled in part by support provided by Compute Canada (www.computeCanada.ca). This work was funded by Canadian Cancer Society (grant #705772) and NSERC RGPIN-2016-06283.

Appendix A. Estimating the dimensions from the tumor bed outline

As a quantitative measure of the tumor extent, Symmans et al. (2007) use the longest diagonal line d_1 inside the tumor bed, and the longest line d_2 within the tumor bed that is perpendicular to d_1 , and combine them in a single quantity $d_{prim} = \sqrt{d_1 d_2}$. After calculating the tumor bed, we compute the convex hull as it simplifies the following calculations, since the convex shape has properties that are easier to deal with than of the tumor bed, which may be an irregular, concave polygon. Furthermore, we can apply $O(n)$ time algorithms to estimate many geometric quantities (such as the diameter of a convex polygon) provided that we have the convex hull (Toussaint, 1983).

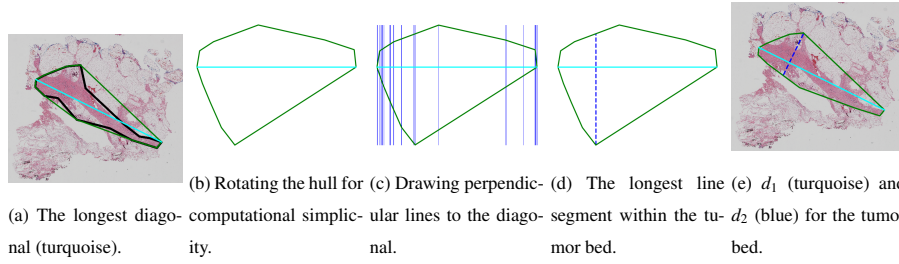


Figure A.3: Extraction of tumor bed extent, d_1 and d_2 , from the convex hull (shown in green on Fig. A.3a) of the tumor bed (shown in black on Fig. A.3a).

Given the convex hull, we first find the longest diagonal d_1 connecting two vertices of the convex hull (Fig. A.3a). Due to the properties of the convex hull, this diagonal is also the maximum extent in the tumor bed. Then, the convex hull is rotated along this longest diagonal using the 2d rotation matrix R_{d_1} is defined as $\begin{bmatrix} \cos\theta & -\sin\theta \\ \sin\theta & \cos\theta \end{bmatrix}$ (Fig. A.3b). Given two endpoints of the longest diagonal (x_1, y_1) and (x_2, y_2) , where the latter point is above the former ($y_2 > y_1$), θ is given by $-\tan^{-1}(\frac{y_2-y_1}{x_2-x_1})$. We use `arctan2` function defined in most programming languages and packages for \tan^{-1} . The resulting transformed hull is used to draw line segments perpendicular to the longest diagonal, crossing each vertex of the hull (Fig. A.3c). After the two crossing points (given that the vertex is not an extreme point on the convex hull) are identified, we pick the longest one as d_2 (Fig. A.3d), which is the longest line segment perpendicular to the original diagonal by the convex hull properties. The process is summarized in Fig. A.3, where we overlaid the resulting dimensions on the original tumor bed for visualization.

References

- Akbar, S., Peikari, M., Salama, S., Panah, A.Y., Nofech-Mozes, S., Martel, A.L., 2019. Automated and manual quantification of tumour cellularity in digital slides for tumour burden assessment. *Scientific Reports* 9, 14099.
- Aresta, G., Araújo, T., Kwok, S., Chennamsetty, S.S., Safwan, M., Alex, V., Marami, B., Prastawa, M., Chan, M., Donovan, M., et al., 2019. Bach: Grand challenge on breast cancer histology images. *Medical image analysis* .

- Bandi, P., Geessink, O., Manson, Q., Van Dijk, M., Balkenhol, M., Hermsen, M., Bejnordi, B.E., Lee, B., Paeng, K., Zhong, A., et al., 2018. From detection of individual metastases to classification of lymph node status at the patient level: the CAMELYON17 challenge. *IEEE Transactions on Medical Imaging* 38, 550–560.
- Campanella, G., Hanna, M., Geneslaw, L., Miraflor, A., Silva, V., Busam, K., Brogi, E., Reuter, V., Klimstra, D., Fuchs, T., 2019. Clinical-grade computational pathology using weakly supervised deep learning on whole slide images. *Nature Medicine* 25, 1. doi:10.1038/s41591-019-0508-1.
- DeSantis, C., Ma, J., Bryan, L., Jemal, A., 2014. Breast cancer statistics, 2013. *CA: a cancer journal for clinicians* 64, 52–62.
- Ehteshami Bejnordi, B., Veta, M., Johannes van Diest, P., van Ginneken, B., Karssemeijer, N., Litjens, G., van der Laak, J.A.W.M., , the CAMELYON16 Consortium, 2017. Diagnostic Assessment of Deep Learning Algorithms for Detection of Lymph Node Metastases in Women With Breast Cancer. *JAMA* 318, 2199–2210.
- Macenko, M., Niethammer, M., Marron, J.S., Borland, D., Woosley, J.T., Guan, X., Schmitt, C., Thomas, N.E., 2009. A method for normalizing histology slides for quantitative analysis, in: 2009 IEEE International Symposium on Biomedical Imaging: From Nano to Macro, IEEE. pp. 1107–1110.
- Martel, A.L., Nofech-Mozes, S., Salama, S., Akbar, S., Peikari, M., 2019. Assessment of residual breast cancer cellularity after neoadjuvant chemotherapy using digital pathology [data set]. <https://doi.org/10.7937/TCIA.2019.4YIBTJNO>.
- Peikari, M., Salama, S., Nofech-Mozes, S., Martel, A.L., 2017. Automatic cellularity assessment from post-treated breast surgical specimens. *Cytometry Part A* 91, 1078–1087.
- Srinidhi, C.L., Ciga, O., Martel, A.L., 2019. Deep neural network models for computational histopathology: A survey. *arXiv preprint arXiv:1912.12378* .
- Symmans, W.F., Peintinger, F., Hatzis, C., Rajan, R., Kuerer, H., Valero, V., Assad, L., Poniecka, A., Hennessy, B., Green, M., et al., 2007. Measurement of residual

breast cancer burden to predict survival after neoadjuvant chemotherapy. *Journal of Clinical Oncology* 25, 4414–4422.

Symmans, W.F., Wei, C., Gould, R., Yu, X., Zhang, Y., Liu, M., Walls, A., Bousamra, A., Ramineni, M., Sinn, B., et al., 2017. Long-term prognostic risk after neoadjuvant chemotherapy associated with residual cancer burden and breast cancer subtype. *Journal of Clinical Oncology* 35, 1049.

Tan, M., Le, Q., 2019. EfficientNet: Rethinking model scaling for convolutional neural networks, in: Chaudhuri, K., Salakhutdinov, R. (Eds.), *Proceedings of the 36th International Conference on Machine Learning*, PMLR, Long Beach, California, USA. pp. 6105–6114. URL: <http://proceedings.mlr.press/v97/tan19a.html>.

Toussaint, G.T., 1983. Solving geometric problems with the rotating calipers, in: *Proc. IEEE Melecon*, p. A10.

Table 2: Binary (tumor vs. no tumor) classification accuracies on BreastPathQ test set under different settings. Unless otherwise stated, test-time augmentations (TTA) are set to two.

Setting	Acc.	Cfs. mtx.
No augmentation	93.5%	$\begin{pmatrix} 186 & 45 \\ 27 & 848 \end{pmatrix}$
Stain norm	92.4%	$\begin{pmatrix} 180 & 51 \\ 32 & 843 \end{pmatrix}$
Color jittering	93.5%	$\begin{pmatrix} 205 & 26 \\ 46 & 829 \end{pmatrix}$
Affine trs.	94.4%	$\begin{pmatrix} 207 & 24 \\ 38 & 837 \end{pmatrix}$
TTA = 1	92.9%	$\begin{pmatrix} 198 & 33 \\ 45 & 830 \end{pmatrix}$
TTA = 2	93.5%	$\begin{pmatrix} 186 & 45 \\ 27 & 848 \end{pmatrix}$
TTA = 3	93.3%	$\begin{pmatrix} 183 & 48 \\ 26 & 849 \end{pmatrix}$
TTA = 4	92.9%	$\begin{pmatrix} 178 & 53 \\ 25 & 850 \end{pmatrix}$
TTA = 16	92.2%	$\begin{pmatrix} 167 & 64 \\ 22 & 853 \end{pmatrix}$
B0	93.5%	$\begin{pmatrix} 186 & 45 \\ 27 & 848 \end{pmatrix}$
B3	93.1%	$\begin{pmatrix} 189 & 42 \\ 34 & 841 \end{pmatrix}$
B5	95.1%	$\begin{pmatrix} 201 & 30 \\ 24 & 851 \end{pmatrix}$
B7	93.5%	$\begin{pmatrix} 193 & 38 \\ 34 & 841 \end{pmatrix}$

Table 3: The effect of sampling negative instances randomly versus a clustering approach. Under each sampling strategy, we compare various methods to handle class imbalance. \propto indicates using class weights in cross-entropy loss directly proportional to class distributions, $=$ uses weights 1 for all classes. Each setting uses the EfficientNet-B0 framework, 256 as the tile stride, and only random cropping as data augmentation.

Negative sam- pling	Weighing	Dice coeffi- cient	Error $\sqrt{d_1 d_2}$	in Confusion matrix
K-means	\propto	0.68	2.82	$\begin{pmatrix} 7 & 7 \\ 2 & 30 \end{pmatrix}$
	$\frac{1}{\propto}$	0.70	3.10	$\begin{pmatrix} 4 & 10 \\ 1 & 31 \end{pmatrix}$
	$=$	0.66	2.70	$\begin{pmatrix} 8 & 6 \\ 1 & 31 \end{pmatrix}$
	Minority oversampling	0.74	2.06	$\begin{pmatrix} 8 & 6 \\ 1 & 31 \end{pmatrix}$
Random	\propto	0.71	3.66	$\begin{pmatrix} 3 & 11 \\ 0 & 32 \end{pmatrix}$
	$\frac{1}{\propto}$	0.69	3.65	$\begin{pmatrix} 3 & 11 \\ 0 & 32 \end{pmatrix}$
	$=$	0.71	2.64	$\begin{pmatrix} 4 & 10 \\ 0 & 32 \end{pmatrix}$
	Minority oversampling	0.74	2.41	$\begin{pmatrix} 5 & 9 \\ 1 & 31 \end{pmatrix}$
None	\propto	0.50	10.60	$\begin{pmatrix} 0 & 14 \\ 0 & 32 \end{pmatrix}$
	$\frac{1}{\propto}$	0.51	10.18	$\begin{pmatrix} 0 & 14 \\ 0 & 32 \end{pmatrix}$
	$=$	0.50	10.44	$\begin{pmatrix} 0 & 14 \\ 0 & 32 \end{pmatrix}$
	Minority oversampling	0.47	11.09	$\begin{pmatrix} 0 & 14 \\ 0 & 32 \end{pmatrix}$

Table 4: The effect of data augmentation on slide-level tasks using the K-means negative sampling strategy, 256 as the tile stride, and EfficientNet-B0 architecture.

Random crop	Stain norm.	Color jittering	Affine trs.	Dice coeff.	Error in $\sqrt{d_1 d_2}$	Cfs. mtx.
				0.72	2.58	$\begin{pmatrix} 5 & 8 \\ 0 & 33 \end{pmatrix}$
✓	✓			0.73	2.03	$\begin{pmatrix} 8 & 6 \\ 1 & 31 \end{pmatrix}$
✓		✓		0.78	1.52	$\begin{pmatrix} 7 & 7 \\ 1 & 31 \end{pmatrix}$
✓			✓	0.78	2.22	$\begin{pmatrix} 9 & 5 \\ 1 & 31 \end{pmatrix}$

Table 5: The effect of architecture size/complexity on slide-level tasks. In all experiments, we use K-means negative sampling, 256 as the tile stride, and only random cropping as data augmentation.

Architecture params)	(#	Dice coeff.	Error in $\sqrt{d_1 d_2}$	Cfs. mtx.
B0 (5M)		0.74	2.06	$\begin{pmatrix} 8 & 6 \\ 1 & 31 \end{pmatrix}$
B3 (12M)		0.78	1.80	$\begin{pmatrix} 9 & 5 \\ 1 & 31 \end{pmatrix}$
B5 (30M)		0.71	1.74	$\begin{pmatrix} 9 & 5 \\ 2 & 30 \end{pmatrix}$
B7 (58M)		0.75	2.25	$\begin{pmatrix} 9 & 5 \\ 0 & 32 \end{pmatrix}$

Table 6: The effect of sliding window tile stride on slide-level tasks using the EfficientNet-B3 architecture. In all experiments, we use K-means negative sampling and only random cropping as data augmentation.

Stride	Dice coefficient	Error in $\sqrt{d_1 d_2}$	Cfs. mtx.
512	0.75	2.18	$\begin{pmatrix} 2 & 12 \\ 0 & 32 \end{pmatrix}$
256	0.78	1.80	$\begin{pmatrix} 9 & 5 \\ 1 & 31 \end{pmatrix}$
128	0.75	2.00	$\begin{pmatrix} 11 & 3 \\ 0 & 32 \end{pmatrix}$
64	0.75	2.02	$\begin{pmatrix} 10 & 4 \\ 0 & 32 \end{pmatrix}$
32	0.74	1.98	$\begin{pmatrix} 9 & 5 \\ 0 & 32 \end{pmatrix}$
16	0.74	2.00	$\begin{pmatrix} 9 & 5 \\ 0 & 32 \end{pmatrix}$

Table 7: Comparison between references (expert pathologists), and our method on slide-level tasks using the EfficientNet-B3 architecture, including the consensus ground truth (with 8% of the dataset removed). P#* indicates the expert ID, and *CNN* is the trained network to segment the tumor bed automatically. In all experiments, we use K-means negative sampling, 128 as the tile stride, and only random cropping as data augmentation.

Reference	Target	Dice coefficient	Error	in Cfs. mtx.
			$\sqrt{d_1 d_2}$	
P#1	CNN	0.74	2.10	$\begin{pmatrix} 9 & 4 \\ 1 & 32 \end{pmatrix}$
	P#2	0.78	2.11	$\begin{pmatrix} 13 & 0 \\ 0 & 33 \end{pmatrix}$
	P#3	0.80	1.63	$\begin{pmatrix} 13 & 0 \\ 0 & 33 \end{pmatrix}$
P#2	CNN	0.73	2.58	$\begin{pmatrix} 9 & 4 \\ 1 & 32 \end{pmatrix}$
	P#3	0.81	1.71	$\begin{pmatrix} 13 & 0 \\ 0 & 33 \end{pmatrix}$
P#3	CNN	0.78	1.31	$\begin{pmatrix} 9 & 4 \\ 1 & 32 \end{pmatrix}$
Consensus	CNN	0.75	2.00	$\begin{pmatrix} 11 & 3 \\ 0 & 32 \end{pmatrix}$
	P#1	0.81	1.46	$\begin{pmatrix} 13 & 1 \\ 0 & 32 \end{pmatrix}$
	P#2	0.84	1.35	$\begin{pmatrix} 13 & 1 \\ 0 & 32 \end{pmatrix}$
	P#3	0.82	1.45	$\begin{pmatrix} 13 & 1 \\ 0 & 32 \end{pmatrix}$

Table 8: Comparison between references (expert pathologists), and our method on slide-level tasks using the EfficientNet-B3 architecture, prior to including consensus ground truth. P#* indicates the expert ID, and CNN is the trained network to segment the tumor bed automatically. In all experiments, we use K-means negative sampling, 128 as the tile stride, and only random cropping as data augmentation.

Reference	Target	Dice coefficient	Error $\sqrt{d_1 d_2}$	in Cfs. mtx.
P#1	CNN	0.71	2.49	$\begin{pmatrix} 9 & 5 \\ 2 & 34 \end{pmatrix}$
	P#2	0.74	2.86	$\begin{pmatrix} 13 & 0 \\ 1 & 36 \end{pmatrix}$
	P#3	0.78	2.00	$\begin{pmatrix} 13 & 0 \\ 1 & 36 \end{pmatrix}$
P#2	CNN	0.71	2.89	$\begin{pmatrix} 9 & 4 \\ 2 & 35 \end{pmatrix}$
	P#3	0.78	1.96	$\begin{pmatrix} 13 & 0 \\ 0 & 37 \end{pmatrix}$
P#3	CNN	0.75	1.33	$\begin{pmatrix} 9 & 4 \\ 2 & 35 \end{pmatrix}$